Received: 6 October 2025 | Accepted: 5 November 2025

DOI: 10.1111/mice.70161

COMPUTER-AIDED CIVIL AND INFRASTRUCTURE ENGINEERING WILEY

RESEARCH ARTICLE

Data-driven dynamic mode decomposition framework for spatio-temporal prediction of concrete chloride ingress

Yue Li | **Miroslav Vořechovský**

Institute of Structural Mechanics, Brno University of Technology, Brno, Czech Republic

Correspondence
Miroslav Vořechovský, Institute of Structural Mechanics, Brno University of Technology, Brno, Czech Republic.
Email: miroslav.vorechovsky@vut.cz

Funding information
European Research Council (ERC), Grant/Award Number: 101167045; Czech Science Foundation, Grant/Award Number: GA24-10892S

Abstract

Prediction of concrete chloride ingress under varying environmental conditions is computationally demanding, particularly when mesostructural effects are considered. Uncertainties in service history and material properties further limit conventional models. This study develops a data-driven dynamic mode decomposition framework for efficient prediction. It decomposes spatio-temporal chloride concentration data into eigenmodes with temporal coefficients for accurate reconstruction and extrapolation. Its performance is demonstrated under constant, annual cyclic, and multi-frequency boundary conditions. The reduced-order representation cuts data storage by over 99% and enhances computational efficiency by over 91%. Sensitivity analyses indicate higher accuracy when input data are collected after long-term chloride ingress and covers sufficient boundary cycles. Linear transformations of surface concentration fluctuations can be directly mapped to temporal coefficients of corresponding oscillatory modes. An analytical model expressing chloride profiles as an explicit function of depth and time is derived, applicable to all scenarios predictable by the proposed method.

1 | INTRODUCTION

Chloride ingress is one of the most critical durability issues in reinforced concrete exposed to seawater, saline spray, or de-icing salts (Papadakis, 2000). It involves chloride ions penetrating the concrete matrix, typically driven by a concentration gradient (Jensen et al., 1999). When these ions reach the reinforcement surface and exceed a critical threshold, depassivation occurs (Glass & Buenfeld, 2000; Strauss et al., 2010), triggering corrosion, cracking, and a loss of structural capacity (Cusson et al., 2011; Kuntal et al., 2021). In the United States, about 173,000 bridges are classified as structurally deficient or functionally obsolete, largely due to chloride-induced corrosion (Radlińska et al., 2014). Globally, the annual economic cost of corrosion was estimated at $2.5 trillion in 2016 (Koch et al., 2016), with a large share attributed to chloride-related deterioration. Consequently, extensive research has focused on understanding and predicting chloride penetration in reinforced concrete.

Chloride ingress models have evolved from analytical to numerical approaches (Nilsson, 2022). The earliest models treated concrete as a homogeneous medium governed by Fick's diffusion law (Bažant, 1979a, 1979b), yielding a one-dimensional solution expressed with the error function (Collepardi et al., 1972). Subsequent studies incorporated time-dependent diffusion parameters (Kim et al., 2016), as well as chloride binding, and convection effects in unsaturated concrete (Ababneh et al., 2003; Tang & Joost, 2007). Finite element methods (Yu & Adeli, 1993) later enabled

numerical solutions that account for material and environmental uncertainties (Bastidas-Arteaga et al., 2011). The original one-dimensional model was extended to two- and three-dimensional forms (Liu et al., 2012). Concrete heterogeneity has since been addressed using multiphase models that explicitly represent aggregates, mortar, and the interfacial transition zone (Qiu & Dai, 2021; Tong et al., 2025). While these methods provide strong physical fidelity, they depend on detailed knowledge of material properties, service history, and exposure conditions. However, such information may not always be available in practice, for example, in existing structures with limited monitoring or where environmental conditions have fluctuated over time.

Emerging computational approaches offer alternatives to conventional Fick's law-based modeling. Šavija et al. (2013, 2014) employed a three-dimensional lattice model to simulate chloride ingress in both sound and cracked concrete, with experimental observations reproduced. Biondini et al. (2004) introduced a cellular automata model capturing ion transport through rule-based local interactions. Recently, various machine learning methods and their integration with finite element models have been explored (Alam et al., 2020; Pereira et al., 2020), especially in predicting the chloride profile with respect to the depth (Cai et al., 2020). However, long-term prediction of spatio-temporal evolution of chloride ingress remains challenging.

To increase the computational efficiency for predicting concrete chloride ingress, this study introduces a data-driven dynamic mode decomposition (DMD) framework. Originally developed by Schmid and Sesterhenn (P. J. Schmid, 2010; P. Schmid & Sesterhenn, 2008), DMD constructs linear reduced-order models of high-dimensional systems and extracts spatio-temporal coherent structures governing the observed data. Conceptually, it provides a coupled representation of spatial and temporal modes, integrating principles of principal component analysis and Fourier transformation. Unlike these methods or the widely used singular value decomposition (SVD), DMD assigns each mode a predetermined damped (or driven) sinusoidal behavior in time. Compared with other data-driven methods, DMD offers physical interpretability by representing each spatial eigenmode in the same physical units as the input data, while the associated temporal coefficients remain dimensionless. This feature not only facilitates physical interpretation but also provides a foundation for future extensions, such as physically informed or reinforced modeling. As an unsupervised method, DMD identifies the low-rank dynamics of large datasets (Viguerie et al., 2022) and has been applied in diverse fields such as fluid dynamics (Bai et al., 2020), epidemiology (Viguerie et al., 2022), and electrical engineering (Mohan et al., 2018). In this work, DMD is applied to predict the spatio-temporal evolution of chloride concentration in concrete. Distinct modes capture underlying mechanisms such as diffusion, convection, and chemical reactions, with the number of retained modes reflecting the system's complexity.

This paper is organized as follows: In Section 2, the method of predicting chloride ingress with DMD is presented. Section 3 contains the simulations of three different cases. Section 4 consists of sensitivity analyses. Finally, the conclusions of the underlying research are presented in Section 5.

2 | COMPUTATIONAL FRAMEWORK

DMD provides the prediction of the behavior of complex physical systems by approximating them as linear dynamical systems. In this framework, the system's state at any time step is expressed as a linear transformation of its state at the previous time step. Given a sequence of system observations, $\boldsymbol{X}_1^N = \{\boldsymbol{x}_1, \boldsymbol{x}_2, \ldots, \boldsymbol{x}_N\}$, where $\boldsymbol{x}_k \in \mathbb{R}^M$ denotes the kth snapshot of the system, and M is the number of spatial points, the data matrix $\boldsymbol{X} \in \mathbb{R}^{M\times N}$ is constructed by stacking these N snapshots as columns. The linear transformation matrix $\boldsymbol{A} \in \mathbb{R}^{M\times M}$ satisfies

$$\boldsymbol{x_k} \approx \boldsymbol{A}\, \boldsymbol{x_{k-1}} \tag{1}$$

Extending this relation to all snapshots gives

$$\boldsymbol{X_2^N} \approx \boldsymbol{A}\, \boldsymbol{X_1^{N-1}} \tag{2}$$

where $\boldsymbol{X}_1^{N-1} = \{\boldsymbol{x}_1, \boldsymbol{x}_2, \ldots, \boldsymbol{x}_{N-1}\}$ and $\boldsymbol{X}_2^N = \{\boldsymbol{x}_2, \boldsymbol{x}_2, \ldots, \boldsymbol{x}_N\}$. If $\boldsymbol{X}_1^{N-1}$ is square and invertible, $\boldsymbol{A}$ is obtained as $\boldsymbol{X}_2^N(\boldsymbol{X}_1^{N-1})^{-1}$. In practice, $\boldsymbol{X}_1^{N-1}$ is rectangular or rank-deficient, and $\boldsymbol{A}$ is estimated as

$$\boldsymbol{A} = \boldsymbol{X}_2^N \left(\boldsymbol{X}_1^{N-1}\right)^{\dagger} \tag{3}$$

where † denotes the Moore–Penrose pseudoinverse (Tu et al., 2014), minimizing the residual of Equation (2). However, $\boldsymbol{A}$ and its pseudoinverse need not be computed explicitly. By substituting the SVD of $\boldsymbol{X}_1^{N-1}$ into Equation (3), the low-dimensional eigenvalues and eigenvectors of $\boldsymbol{A}$ can be efficiently obtained. These eigenvectors define spatial modes associated with characteristic temporal behaviors, oscillatory, exponentially growing or decaying, or combinations thereof. The subsequent section will elaborate on this procedure in the context of predicting concrete chloride ingress.

2.1 | Prediction of chloride ingress using DMD

Predicting chloride ingress in concrete involves forecasting the evolution of ion concentration distribution within the material. The analyzed concrete domain is discretized into M spatial locations, with x_j denoting the jth location, $j \in \{1, 2, \dots, M\}$. The analyzed time interval $[t_{\text{start}},\ t_{\text{predicted}}]$ is presented by N_{all} evenly spaced time points with resolution, $\Delta t = (t_{\text{predicted}} - t_{\text{start}})/(N_{\text{all}} - 1)$. The kth time instant is $t_k = t_{\text{start}} + (k-1)\Delta t,\ k \in \{1, 2, \dots, N_{\text{all}}\}$. The objective is to predict the chloride concentration $c(x_j, t_k)$ at all spatial and temporal points. Notably, throughout this paper, the spatial and temporal indices j and k are consistently used to represent spatial locations and time steps, respectively, as well as related quantities in the spatio-temporal evolution of chloride concentration.

A time-series dataset of chloride concentration over the first N snapshots is required. Since DMD is data-driven, it relies solely on these snapshots rather than on material or environmental parameters. This input dataset spans the time interval $[t_{\text{start}}, t_{\text{end}}]$, with $t_{\text{end}} = t_{\text{start}} + (N-1)\Delta t$. For structures exposed to a salinity environment or specimens exposed to an idealized laboratory environment, chloride concentration can be measured continuously at M locations and N time points, which is convenient with the advanced sensing technologies, like anode ladder or array systems (Torres-Luque et al., 2014; Xiao et al., 2025). Alternatively, if direct measurements are unavailable, validated numerical simulations can provide similar datasets. Following a certain order of spatial locations without missing any location, each snapshot is a vector $\boldsymbol{c}_k = \{c(x_1, t_k),\ c(x_2, t_k), \dots, c(x_M, t_k)\}^{\mathrm{T}} \in \mathbb{R}^M$, where $k \in \{1, 2, \dots, N\}$. The full dataset forms the matrix $\boldsymbol{C}_1^N = \{\boldsymbol{c}_1, \boldsymbol{c}_2, \dots, \boldsymbol{c}_N\} \in \mathbb{R}^{M \times N}$. Analogous to Equation (2), the DMD approximation for chloride ingress becomes

$$\boldsymbol{C}_2^N \approx \boldsymbol{A}\boldsymbol{C}_1^{N-1} \tag{4}$$

where the sub-matrices, $\boldsymbol{C}_1^{N-1}$ and $\boldsymbol{C}_2^N$, are defined as

$$\boldsymbol{C}_1^{N-1} = \{\boldsymbol{c}_1, \boldsymbol{c}_2, \cdots, \boldsymbol{c}_{N-1}\},\ \boldsymbol{C}_2^N = \{\boldsymbol{c}_2, \boldsymbol{c}_3, \cdots, \boldsymbol{c}_N\} \tag{5}$$

To extract dominant spatio-temporal patterns, the SVD of $\boldsymbol{C}_1^{N-1}$ is performed. The SVD of $\boldsymbol{C}_1^{N-1}$ is given by:

$$\boldsymbol{C}_1^{N-1} = \boldsymbol{U}\,\boldsymbol{\Sigma}\,\boldsymbol{V}^{\mathrm{T}} \tag{6}$$

where $\boldsymbol{U} \in \mathbb{R}^{M \times M}$ and $\boldsymbol{V}^{\mathrm{T}} \in \mathbb{R}^{(N-1)\times(N-1)}$ are two unitary matrices containing orthonormal spatial modes in columns and orthonormal temporal modes in rows, respectively, and $\boldsymbol{\Sigma} \in \mathbb{R}^{M \times (N-1)}$ is a diagonal matrix with non-negative singular values $\sigma_{s,s}$, in descending order by index s and quantifying the energy or significance of each mode. To retain most of the system's dynamics, the decomposition is truncated at rank $r \le \min\{M, N-1\}$:

$$r = \underset{r}{\operatorname{argmin}} \left\{ 1 - \frac{\sum_{s=1}^{r} \sigma_{s,s}}{\sum_{s=1}^{\min\{M,N-1\}} \sigma_{s,s}} \le \varepsilon \right\} \tag{7}$$

where ϵ defines the maximum allowable loss of information. It is initially set as 10^{-3}, followed by a sensitivity analysis in later sections. This truncation yields the compact SVD:

$$\boldsymbol{C}_1^{N-1} \approx \boldsymbol{U}_r\,\boldsymbol{\Sigma}_r\,\boldsymbol{V}_r^{\mathrm{T}} \tag{8}$$

where $\boldsymbol{U}_r$ includes the first r columns of $\boldsymbol{U}$, $\boldsymbol{\Sigma}_r$ is the $r \times r$ principal sub-matrix of $\boldsymbol{\Sigma}$, and $\boldsymbol{V}_r^{\mathrm{T}}$ consists of the fist r rows of $\boldsymbol{V}^{\mathrm{T}}$. Although this representation captures the dominant modes of chloride transport, the temporal coefficients in $\boldsymbol{V}_r^{\mathrm{T}}$ are not yet suitable for direct prediction due to their complex evolution.

An order-reduced matrix $\tilde{\boldsymbol{A}}$ related to the high-dimensional linear operator $\boldsymbol{A}$ via similarity transformation is formed in the third step, and it is analyzed to get the eigenvectors and eigenvalues of $\boldsymbol{A}$. Substituting Equation (8) into Equation (4) yields

$$\boldsymbol{C}_2^N \approx \boldsymbol{A}\,\boldsymbol{U}_r\,\boldsymbol{\Sigma}_r\,\boldsymbol{V}_r^{\mathrm{T}} \tag{9}$$

Left-multiplying the both sides of Equation (9) above by $\boldsymbol{U}_r^{\mathrm{T}}$ and then right-multiplying them by $\boldsymbol{V}_r\boldsymbol{\Sigma}_r^{-1}$ gives

$$\boldsymbol{U}_r^{\mathrm{T}}\,\boldsymbol{C}_2^N\,\boldsymbol{V}_r\,\boldsymbol{\Sigma}_r^{-1} \approx \boldsymbol{U}_r^{\mathrm{T}}\,\boldsymbol{A}\,\boldsymbol{U}_r \tag{10}$$

The right side of Equation (10) is defined as $\tilde{\boldsymbol{A}} \in \mathbb{R}^{r \times r}$, and it is a low-dimensional representation of the system dynamics. $\tilde{\boldsymbol{A}}$ is equivalent to the matrix $\boldsymbol{A} \in \mathbb{R}^{M \times M}$ projected into a much smaller r-dimensional subspace via the linear transformation matrix, $\boldsymbol{U}_r$. To understand the time evolution of the dominant modes, an eigen-decomposition is performed on $\tilde{\boldsymbol{A}}$:

$$\tilde{\boldsymbol{A}}\,\boldsymbol{W} = \boldsymbol{W}\,\boldsymbol{\Lambda} \tag{11}$$

where $\boldsymbol{W} \in \mathbb{R}^{r \times r}$ contains the eigenvectors $\boldsymbol{w}_s$ and $\boldsymbol{\Lambda} \in \mathbb{R}^{r \times r}$ is a diagonal matrix with eigenvalues λ_s ordered by index s:

$$\boldsymbol{W} = \{\boldsymbol{w}_1, \boldsymbol{w}_2, \cdots, \boldsymbol{w}_r\},\ \boldsymbol{\Lambda} = \begin{bmatrix} \lambda_1 & 0 & \cdots & 0 \\ 0 & \lambda_2 & \cdots & 0 \\ \vdots & \vdots & \ddots & \vdots \\ 0 & 0 & \cdots & \lambda_r \end{bmatrix} \tag{12}$$

Notably, the eigen-decomposition in Equation (11) yields $\boldsymbol{W}$ and $\boldsymbol{\Lambda}$ as complex matrices so as the subsequent quantities derived from them. However, their complex elements appear conjugate pairs with their neighbors, sharing identical real parts and symmetric imaginary parts. Consequently, the predicted ion concentrations are guaranteed to be purely real values.

The high-dimensional DMD modes and the associated evolution of the temporal coefficients are obtained in the fourth step to form the prediction of the spatio-temporal evolution of the chloride concentration distribution. The DMD eigenmodes, $\boldsymbol{\Phi} \in \mathbb{R}^{M\times r}$, are obtained by lifting the order-reduced eigenvectors:

$$\boldsymbol{\Phi} = \boldsymbol{U}_r \boldsymbol{W} = \boldsymbol{C}_2^N \boldsymbol{V}_r \boldsymbol{\Sigma}_r^{-1} \boldsymbol{W} \tag{13}$$

Each column $\boldsymbol{\phi}_s \in \mathbb{R}^M$ of $\boldsymbol{\Phi}$ represents a characteristic spatial mode of chloride concentration distribution on the M spatial locations. These modes are mostly complex, automatically normalized but not orthogonal. The chloride concentration at any time point t_k is predicted as

$$\boldsymbol{c}_{\mathrm{DMD}}(t_k) = \boldsymbol{\Phi}\boldsymbol{\Lambda}^{k-1}\boldsymbol{b}, \quad \boldsymbol{k} \in \{1, 2, \cdots, N_{\mathrm{all}}\} \tag{14}$$

where $\boldsymbol{b}$ is the complex vector describing the initial amplitudes of DMD eigenmodes at time t_{start}, and $\boldsymbol{\Lambda}^{k-1}\boldsymbol{b}$ is the vector containing the temporal coefficient of these eigenmodes at the kth snapshot. Equating k in Equation (14) to one yields the sought value of $\boldsymbol{b}$:

$$\boldsymbol{b} = \boldsymbol{\Phi}^{\dagger}\boldsymbol{c}_1 \tag{15}$$

where $\boldsymbol{\Phi}^{\dagger}$ is the Moore–Penrose pseudoinverse of $\boldsymbol{\Phi}$. As a result, Equation (14) allows the reconstruction of known concentration distribution for $k \leq N$ and the prediction of the unknown distribution for $k > N$. To convert the temporal coefficients for discrete time snapshots to the ones for continuous time, an r-rank diagonal complex matrix $\boldsymbol{\Omega} = \mathrm{diag}(\omega_1, \omega_2, \ldots, \omega_r)$ is defined with

$$\omega_s = \ln(\lambda_s)/\Delta t \tag{16}$$

Inserting Equation (16) into Equation (14) gives the continuous-time prediction of chloride concentration:

$$\begin{aligned} c_{\mathrm{DMD}}(t) &= \boldsymbol{\Phi}\, e^{\boldsymbol{\Omega}(t-t_{\mathrm{start}})}\boldsymbol{b} \\ &= \boldsymbol{\Phi}\, e^{\mathrm{re}(\boldsymbol{\Omega})(t-t_{\mathrm{start}})}[\cos(\mathrm{im}(\boldsymbol{\Omega})(t-t_{\mathrm{start}})) \\ &\quad + i\,\sin(\mathrm{im}(\boldsymbol{\Omega})(t-t_{\mathrm{start}}))]\,\boldsymbol{b} \end{aligned} \tag{17}$$

where re(·) and im(·) denote the real and imaginary parts, respectively. Therefore, $e^{\boldsymbol{\Omega}(t-t_{\mathrm{start}})}$ in Equation (17) represents a damped oscillatory complex coefficient, expressed as the product of a real exponential function and a complex oscillation function. The positive or negative real part of ω_s indicates the growth or decay rate of the sth DMD eigenmode, and the non-zero imaginary part indicates the corresponding oscillation frequency. Similar to $\boldsymbol{W}$ and $\boldsymbol{\Lambda}$ in Equation (11), the elements of $\boldsymbol{\Phi}$ and $e^{\boldsymbol{\Omega}(t-t_{\mathrm{start}})}$ are either purely real or appear in complex conjugate pairs, ensuring that the obtained ion concentrations in $\boldsymbol{c}_{\mathrm{DMD}}(t)$ remain purely real values. As the obtained eigenmodes in $\boldsymbol{\Phi}$ are already automatically normalized, the magnitudes of the temporal coefficients of a single mode or of a complex conjugate pair quantitatively indicate their contribution to the predicted concentration distribution. Notably, the presence of complex conjugate pairs indicates that ion concentration evolution is partly described by temporally oscillatory modes. However, such fluctuations in temporal coefficients do not necessarily originate from oscillations in boundary conditions, as solutions with time-invariant boundary conditions may also contain complex components. For such complex conjugate pairs, the real parts of $\boldsymbol{\Omega}$ are usually non-positive, implying that these oscillatory modes decay, although sometimes at a very slow rate. Additionally, the predicted $c_{\mathrm{DMD}}(t)$ is not guaranteed to remain non-negative in this approach, which should be verified and mitigated, for example, by refining the time steps between temporal snapshots.

3 | NUMERICAL EXAMPLE: PREDICTION OF CHLORIDE CONCENTRATION EVOLUTION IN CONCRETE

3.1 | Setup of the three cases

Three cases, denoted as Case-I, Case-II, and Case-III, are analyzed to assess the proposed method's performance in predicting chloride ingress in concrete over 100 years. These correspond to (i) constant, (ii) annual cyclic, and (iii) multi-frequency cyclic (annual and monthly) boundary conditions. All analyses will be performed with the mesostructure of concrete explicitly resolved, providing detailed two-dimensional chloride concentration distributions. This is essential for capturing uncertainties in chloride ingress caused by material heterogeneity. From an engineering perspective, prediction accuracy will be evaluated based on depth-wise concentration profiles, and the effect of heterogeneity will be further discussed in the following section.

A two-dimensional concrete model of 0.3 × 0.1 m, see Figure 1a is employed. The two-phase mesostructure consists of impermeable polygonal coarse aggregates embedded in a permeable mortar matrix, which represents a homogenized mixture of fine aggregates and cement

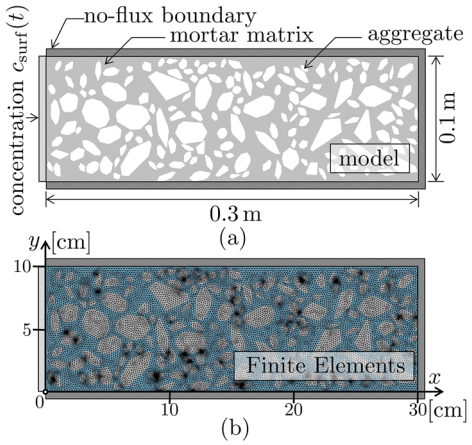

FIGURE 1 (a) Mesoscale concrete model with a prescribed surface concentration $c_{surf}(t)$ on the left boundary. (b) Finite element discretization with maximum element size of 2 mm.

paste. The coarse aggregate area fraction, size range, and gradation are set to 41.4%, 5 to 25 mm, and the standard Fuller distribution, respectively, and their axial ratio, longest-to-shortest axis, follows a general extreme value distribution with the location parameter of 1.61, the scale parameter of 0.46, and the shape parameter of 0.28 (Ruan et al., 2019). Aggregates are generated according to these distributions until the target area fraction is reached, shaped into polygons by stretching, and placed without overlapping each other or penetrating the model boundary.

Chloride transport is governed by Fick's law (Dhir et al., 1998). Initially, the model is chloride-free, that is, $c(x, t_{start}) = 0$. The chloride concentration in the mortar phase evolves as

$$\frac{\partial c(x,t)}{\partial t} = \frac{\partial}{\partial x}\left(-D_{mor}\frac{\partial c(x,t)}{\partial x}\right) \tag{18}$$

where D_{mor} is the diffusion coefficient in mortar. Based on the measured effective diffusion coefficient of concrete (3.37×10^{-6} mm^2/s) according to Zhao et al. (2013) and using a multiscale homogenization approach (Angle et al., 2013; Niklasson et al., 1981), D_{mor} is calibrated to 6.94×10^{-6} mm^2/s.

The boundary condition of the simulations in three cases is different on the left surface of the model. For Case-III, the surface concentration represents a simplified tidal exposure condition in Hangzhou Bay (Zhao et al., 2013), where the environmental exposure fluctuates monthly between seawater and river water, and the ion concentration in seawater fluctuates annually. Thus, the concentration on the model boundary peaks from 0.58% in winter to 0.87% in summer, with an annual minimum of 0%. The concrete is assumed to be saturated, and the potential effects of humidity variation are not considered herein.

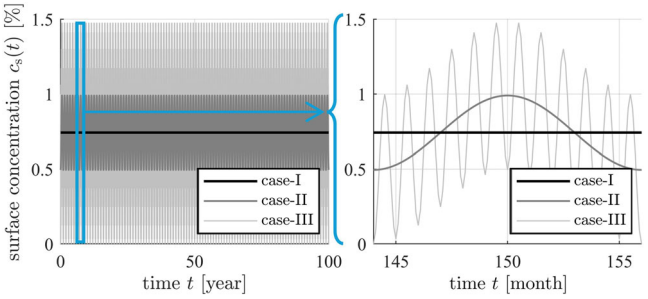

FIGURE 2 Prescribed surface chloride concentration $c_{surf}(t)$ for Case-I (black), Case-II (bold gray), and Case-III (thin gray).

The annual mean value of the concentration in Case-III defines the boundary for case-I, while its monthly mean value defines that for Case-II, see Figure 2:

$$c_{surf,I}(t) \equiv \frac{0.435\%}{1 - 41.4\%} \tag{19}$$

$$c_{surf,II}(t) = \frac{0.435\% - 0.145\%\cos\left(\frac{2\pi t}{\Delta t_{year}}\right)}{1 - f_{agg}^{con}} \tag{20}$$

$$c_{surf,III}(t) = \frac{1}{1-f_{agg}^{con}}\left[0.435\% - 0.145\%\cos\left(\frac{2\pi t}{\Delta t_{year}}\right) - 0.29\%\cos\left(\frac{2\pi t}{\Delta t_{month}}\right)\right] \tag{21}$$

where $1/(1 - 41.4\%)$ is a scaling factor for converting concrete-related ion concentration to the mortar-related concentration, Δt_{year} is the duration of one year, and Δt_{month} is the duration of one month ($\Delta t_{month} = \Delta t_{year}/12$). All other surfaces are assigned no-flux boundary conditions, that is, $\partial c(x,t)/\partial x = 0$.

For numerical implementation, the domain is discretized into triangular finite elements, see Figure 1b. The mesh is refined near aggregate-mortar interfaces, with a maximum element size of 2 mm. The 100-year service life is divided into 12,000 uniform time steps (0.1 month each). Finite element analyses are performed by solving partial differential equations (PDE) in a commercial software on a workstation equipped with an AMD Ryzen 9 5950X CPU and 64 GB RAM, while DMD prediction is conducted in MATLAB R2024b.

3.2 | Case-I: Simulation with constant boundary condition

The data of chloride ingress over a 100-year period are computed using a traditional finite element simulation, where the surface concentration of chloride ions on the left edge of the model, $c_{surf}(t)$, is constantly equal to 0.74%, see Equation (19). Chloride penetrates rapidly during the

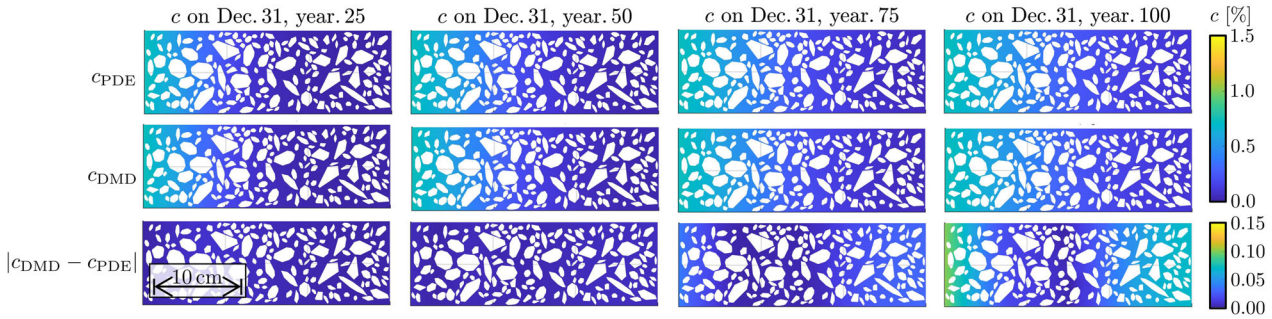

(a) chloride concentration from the traditional method, the DMD method, and the absolute difference between them

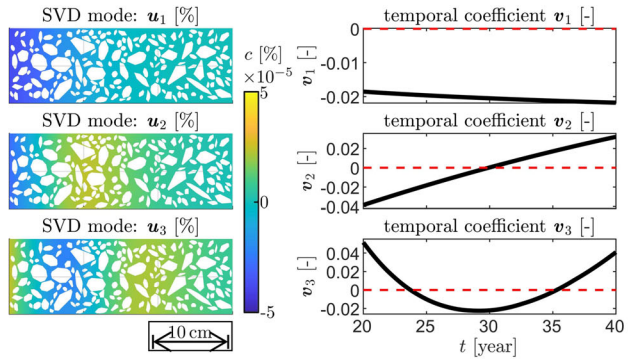

(b) first three modes in the SVD of case-I

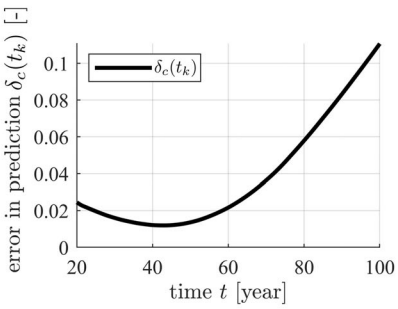

(e) prediction error $\delta_c(t)$ in case-I

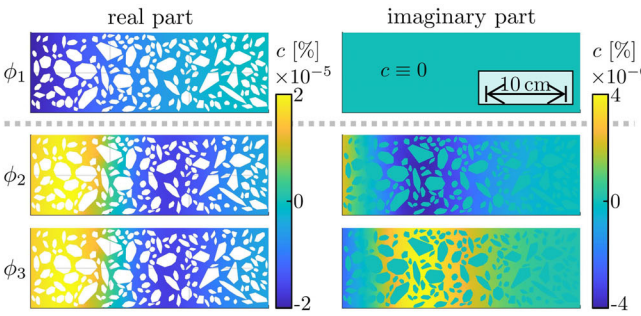

(c) DMD eigenmodes in the prediction of case-I

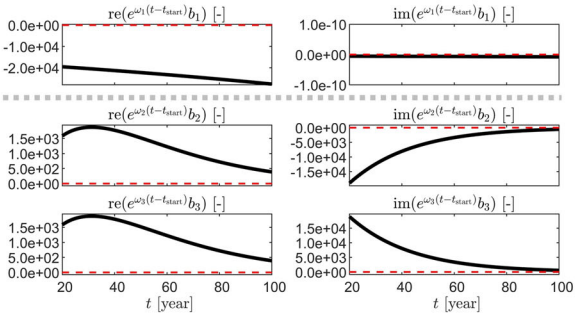

(d) DMD temporal coefficients in the prediction of case-I

FIGURE 3 Analysis of Case-I: (a) comparison of concentration distribution between the data and the prediction, (b) results of the singular value decomposition (SVD), (c) dynamic mode decomposition (DMD) eigenmodes, (d) DMD temporal coefficients, and (e) prediction error $\delta_c(t_k)$.

first 20 years, leading to a sharp concentration increase near the surface, followed by a significant slowdown, see Figure 3a. The complete dataset comprises chloride concentrations at 10,298 spatial nodes of the mortar matrix across 9601 temporal snapshots. For the prediction, a subset of 2401 snapshots from the 20th year to the 40th year is used ($t_{\text{end}} = 40$ year, $N = 2401$), while the following part of the data is stored for validation later on. The influence of using more or fewer data will be examined in the discussion. The selected data are assembled into a matrix $\boldsymbol{C}_1^{2401} \in \mathbb{R}^{10298\times2401}$, where each column represents one snapshot arranged chronologically. Two sub-matrices are constructed as $\boldsymbol{C}_1^{2400}$ and $\boldsymbol{C}_2^{2401}$ according to Equation (5).

To extract the dominant spatio-temporal features of chloride transport, $\boldsymbol{C}_1^{2400}$ was decomposed by SVD with an energy-loss threshold of $\epsilon = 10^{-3}$, yielding a truncated rank $r = 3$. The leading singular values were 9.74×10^5, 5.88×10^4, and 3.78×10^3, indicating a rapid decay in modal energy and confirming that the system dynamics are dominated by the first few modes. The compact SVD is expressed as $\boldsymbol{C}_1^{2400} \approx \boldsymbol{U}_3\,\boldsymbol{\Sigma}_3\,\boldsymbol{V}_3^{\mathrm{T}}$, where $\boldsymbol{\Sigma}_3$ is a 3×3 diagonal matrix of singular values, and $\boldsymbol{U}_3$ and $\boldsymbol{V}_3^{\mathrm{T}}$ contain the corresponding dominant spatial modes and temporal coefficients, respectively, see Figure 3b. It is evident that the temporal coefficients obtained from SVD are too complex to allow direct forecasting. Substituting $\boldsymbol{U}_3$, $\boldsymbol{\Sigma}_3$, and

$\boldsymbol{V}_3$ into Equation (10) gives the order-reduced matrix $\tilde{\boldsymbol{A}}$. Its eigen-decomposition according to Equation (11) yields the eigenvalues $\boldsymbol{\Lambda}$ and eigenvectors $\boldsymbol{W}$. They, together with $\boldsymbol{\Sigma}_3$ and $\boldsymbol{U}_3$, are used in Equations (13)–(16) to obtain the DMD eigenmodes $\boldsymbol{\Phi}$, see Figure 3c, the vector of initial amplitudes $\boldsymbol{b}$:

$$\boldsymbol{b} = \begin{pmatrix} -1.95 \\ 0.158 - 1.89i \\ 0.158 + 1.89i \end{pmatrix} \times 10^4, \ \boldsymbol{b} \in \mathbb{R}^{3\times 1} \tag{22}$$

and the matrix of growth ratio, $\boldsymbol{\Omega}$, in unit of rad/month:

$$\boldsymbol{\Omega} = \mathrm{diag} \begin{pmatrix} 0.362 \\ -3.50 + 0.600i \\ -3.50 - 0.600i \end{pmatrix} \times 10^{-3}, \ \boldsymbol{\Omega} \in \mathbb{R}^{3\times 3} \tag{23}$$

The temporal coefficients $e^{\boldsymbol{\Omega}(t-t_{\mathrm{start}})}\boldsymbol{b}$ of these DMD eigenmodes are evaluated according to Equation (17) with $t \in [10\,\mathrm{year}, 100\,\mathrm{year}]$, see Figure 3d. The first eigenmode represents gradual chloride buildup concentrated near the surface, while the second and third form a complex conjugate pair with identical real and opposite imaginary parts, ensuring real-valued predictions. Their strong similarity indicates possible computational redundancy, further discussed later. As a result, the predicted chloride concentration c_{DMD} agrees well with the finite element results c_{PDE}, see Figure 3a.

The spatial prediction error is evaluated by the absolute difference $|c_{\mathrm{DMD}} - c_{\mathrm{PDE}}|$. It occurs mainly near the exposed surface and deeper regions and increases slightly over time, see the third row of Figure 3a. However, the maximum error, 0.1%, remains much smaller than the surface concentration of 0.74%.

The temporal prediction error is evaluated using the mean absolute error (MAE) on a depth-time grid. At each snapshot, the ion concentration on spatial points obtained from the PDE-based solution and the DMD-based prediction are divided into 300 uniform depth subintervals from 0 to 0.3 m with identical width of 1 mm. The center of the jth subinterval is denoted as $d_j = (j - 0.5)\,\mathrm{mm}$ with $j \in \{1, 2, \ldots, 300\}$. The mean concentration within each depth subinterval and time step forms the depth-time grids of $c_{\mathrm{PDE},d}(d_j, t_k)$ for data from traditional solution and of $c_{\mathrm{DMD},d}(d_j, t_k)$ for prediction with DMD. The time-dependent MAE is computed as.

$$\mathrm{MAE}\,(t_k) = \frac{\sum_{j=1}^{300} \left| c_{\mathrm{DMD},d}\,(d_j, t_k) - c_{\mathrm{PDE},d}\,(d_j, t_k) \right|}{300} \tag{24}$$

For normalization, the average concentration from the data at each time step reads as

$$c_{\mathrm{PDE},d,\mathrm{mean}}\,(t_k) = \frac{\sum_{j=1}^{300} c_{\mathrm{PDE},d}\,(d_j, t_k)}{300} \tag{25}$$

The normalized error $\delta_c(t_k)$, defined as

$$\delta_c\,(t_k) = \frac{\mathrm{MAE}\,(t_k)}{c_{\mathrm{PDE},d,\mathrm{mean}}\,(t_k)} \tag{26}$$

equals zero for perfect prediction and approaches one when the predicted concentrations vanish. The error, $\delta_c(t_k)$, decreases from 0.025 on the 20th year to 0.012 on the 40th year, and then continuously increases to 0.110 on the 100th year, see Figure 3e. For the last 60 years, with the chloride ingress unknown, the complex influence of concrete mesostructure is considered, and the error of predicting the result is generally limited within 10%.

The computational efficiency of the method is evaluated. In terms of data compression, the essential data describing the chloride ingress from the 20th year to the 100th year are extracted from a matrix of size 10,298 × 9601 to two complex matrices of sizes 10,298 × 3 and 3 × 9601, respectively, achieving a 99.88% reduction in data size with preserved accuracy. In terms of memory usage, the PDE-based solution uses 1645 MB of memory, while the DMD-based solution uses 14,071 MB. Both of them are well within available resources. The higher memory usage with Matlab is likely due to its internal computational strategy. In terms of time consumption, the PDE-based solution takes 87 s, whereas the DMD-based solution requires only 7 s, achieving a 91% reduction in computation time.

3.3 | Case-II: Simulation with annual cyclic boundary condition

The data of concrete chloride ingress under an annual cyclic boundary condition over 100 years are prepared in a manner analogous to Case-I. The evolution of surface concentration, $c_{\mathrm{surf}}(t)$, is set according to Equation (20). As a result, the ion concentration close to the left edge exhibits a periodic fluctuation following the environmental changes, while ions continuously penetrate deeper into the concrete away from the boundary, leading to a gradual increase in concentration, see Figure 4a. The matrix $\boldsymbol{C}_1^{2401}$ is organized and analyzed following the same procedure as in Case-I.

Decomposition of $\boldsymbol{C}_1^{2401}$ provides $\boldsymbol{C}_1^{2400} \approx \boldsymbol{U}_4\boldsymbol{\Sigma}_4\boldsymbol{V}_4^{\mathrm{T}}$ according to Equations (6) and (7) with $\epsilon = 10^{-3}$ and resulting $r = 4$. The eigen-decomposition of $\tilde{\boldsymbol{A}}$, according to Equation (10) and (11), and inserting its results into Equations (13)–(16) yields four DMD eigenmodes, see

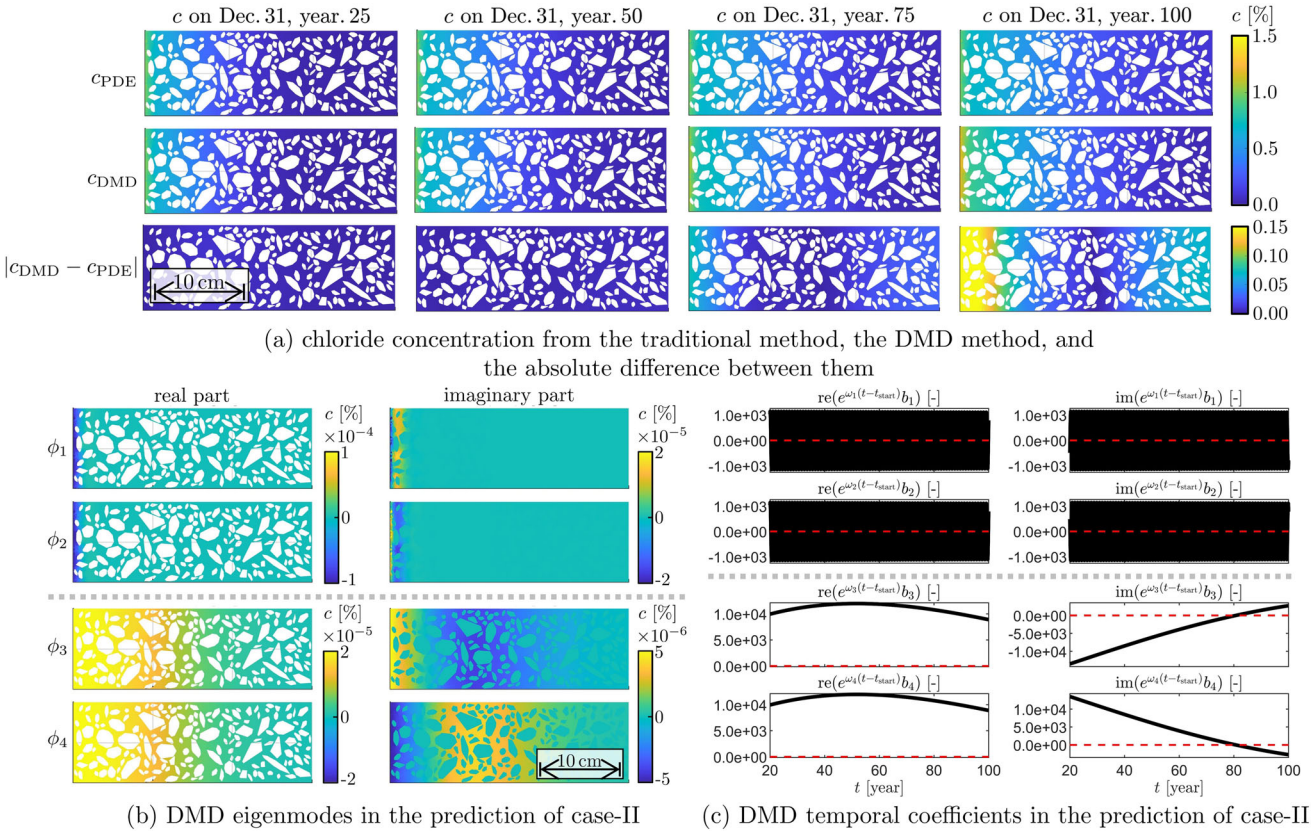

(a) chloride concentration from the traditional method, the DMD method, and the absolute difference between them

(b) DMD eigenmodes in the prediction of case-II

(c) DMD temporal coefficients in the prediction of case-II

FIGURE 4 Analysis of Case-II: (a) comparison of concentration distribution between the data and the prediction, (b) DMD eigenmodes, and (c) DMD temporal coefficients.

Figure 4b, the vector of initial amplitudes $\boldsymbol{b}$:

$$\boldsymbol{b} = \begin{pmatrix} 1.04 - 0.488i \\ 1.04 + 0.488i \\ 9.96 - 13.5i \\ 9.96 + 13.5i \end{pmatrix} \times 10^3, \ \boldsymbol{b} \in \mathbb{R}^{4\times 1} \tag{27}$$

and the matrix of growth ratio, $\boldsymbol{\Omega}$, in unit of rad/month:

$$\boldsymbol{\Omega} = \mathrm{diag} \begin{pmatrix} 523i \\ -523i \\ -0.600 + 1.30i \\ -0.600 - 1.30i \end{pmatrix} \times 10^{-3}, \ \boldsymbol{\Omega} \in \mathbb{R}^{4\times 4} \tag{28}$$

The temporal coefficient $e^{\boldsymbol{\Omega}(t-t_{\text{start}})}\boldsymbol{b}$ is computed according to Equation (17) with $t \in [10\,\text{year}, 100\,\text{year}]$, see Figure 4c. The first two eigenmodes form a complex conjugate pair, with the same real and symmetric imaginary parts. Their eigenvalues, ω_1 and ω_2, are purely imaginary, corresponding to purely oscillatory modes, both sharing a frequency of one cycle per 12 months ($0.52\,\text{month}^{-1} = 2\pi/(12\,\text{months})$). These two modes describe the periodic fluctuation of chloride concentration within approximately 2 cm of the left boundary. The third and fourth modes form a complex conjugate pair that captures the concentration evolution driven by chloride ion diffusion. The product of their complex eigenmodes and temporal coefficients equals the difference between the products of their real and imaginary components. The eigenmode distributions show that the former primarily affects the shallow region, while the latter influences the inner region.

The predicted chloride concentration distribution is obtained according to Equation (17), see Figure 4a. The progressive ingress of chloride ions and the seasonal fluctuation of concentration near the surface are captured by the prediction, with good agreement, compared to the data obtained from the traditional method.

The spatial prediction error occurs mainly near the exposed surface and increases over time, see also Figure 4a. The maximum error over 0.15% is markedly larger than that in Case-I.

The temporal prediction error $\delta_c(t_k)$ decreases from 0.034 on the 20th year to 0.013 on the 34th year, and then continuously increases to 0.379 on the 100th year, see Figure 5. The error tends to increase with the temporal distance from the input data used for prediction, and factors to improve the accuracy will be discussed later.

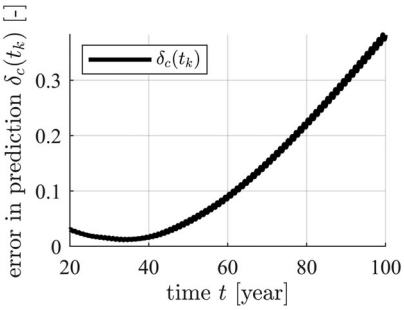

FIGURE 5 Prediction error $\delta_c(t_k)$ over time in Case-II.

The computational efficiency of the method is evaluated. In terms of data compression, the essential information in a matrix of size 10,298 × 9601 is replaced by two complex matrices of size 10,298 × 4 and 4 × 9601, respectively, and the data size is reduced by 99.84%. In terms of memory usage, the PDE-based solution uses 1630 MB of memory usage, while the DMD-based solution uses 14214 MB. In terms of time consumption, the PDE-based solution takes 206 s, whereas the DMD-based solution requires only 7 s, achieving a 97% reduction in computation time.

3.4 | Case-III: Simulation with multi-frequency cyclic boundary condition

The data of concrete chloride ingress under a multi-frequency cyclic boundary condition over 100 years are prepared in the same manner as Case-I and Case-II. The evolution of surface concentration, $c_{\text{surf}}(t)$, is set according to Equation (21). As a result, the ion concentration close to the left edge fluctuates monthly and annually, while in the region away from the left boundary, the ions continuously penetrate rightward, which induces the increase of local concentration, see Figure 6a. The matrix $\boldsymbol{C}_1^{2401}$ is organized and analyzed following the same procedure as in the previous cases.

Decomposition of $\boldsymbol{C}_1^{2401}$ yields $\boldsymbol{C}_1^{2400} \approx \boldsymbol{U}_7\boldsymbol{\Sigma}_7\boldsymbol{V}_7^{\mathrm{T}}$ in this case according to Equations (6) and (7) with $\epsilon = 10^{-3}$ and resulting $r = 7$. The eigen-decomposition of $\tilde{\boldsymbol{A}}$, according to Equation (10) and (11), and inserting its results into Equations (13)–(16) yields four DMD eigenmodes, see Figure 6b, the vector of initial amplitudes $\boldsymbol{b}$:

$$\boldsymbol{b} = \begin{pmatrix} -0.904 + 1.14i \\ -0.904 - 1.14i \\ -1.17 + 0.176i \\ -1.17 - 0.176i \\ -17.7 \\ -0.807 + 7.54i \\ -0.807 - 7.54i \end{pmatrix} \times 10^3,\ \boldsymbol{b} \in \mathbb{R}^{7\times 1} \tag{29}$$

and the matrix of growth ratio, $\boldsymbol{\Omega}$, in unit of rad/month:

$$\boldsymbol{\Omega} = \operatorname{diag}\begin{pmatrix} -0.600 + 6280i \\ -0.600 - 6280i \\ -0.400 + 524i \\ -0.400 - 524i \\ 0.505 \\ -3.30 + 150i \\ -3.30 - 150i \end{pmatrix} \times 10^{-3},\ \boldsymbol{\Omega} \in \mathbb{R}^{7\times 7} \tag{30}$$

The temporal coefficient $e^{\boldsymbol{\Omega}(t-t_{\text{start}})}\boldsymbol{b}$ is computed according to Equation (17) with $t \in [10\,\text{year}, 100\,\text{year}]$, see Figure 6c. The first two modes present slow-decayed oscillation and share a frequency of one cycle per month (6.28/month = 2π/(1 month)), contributing to describing the temporal fluctuation of concentration within the depth of less than 1 mm from the left edge of the model. The third and fourth modes present slow-decayed oscillation, share a frequency of one cycle per year, and contribute to the temporal fluctuation within the depth of 2 cm from the left edge. The fifth mode only has the real part in the spatial distribution of concentration and in the temporal coefficient. The sixth and seventh modes are a pair of slow decay ones, which describe the cumulative inward diffusion of chloride ions together with the fifth mode. Three pairs of complex conjugate modes share identical real parts and symmetric imaginary parts in both spatial modes and temporal coefficients. To simplify the computation, the merging of these pairs will be discussed in the following section.

The prediction result is obtained according to Equation (17), see Figure 6a. The predicted evolution of concentration distribution exhibits the monthly and annual fluctuations of chloride concentration close to the left edge of the model and the continuous increase in concentration in the deeper part of the model.

The spatial prediction error occurs mainly in the region near but not connected with the exposed surface and increases over time, see also Figure 6a. The maximum error 0.13% is considerably smaller than the maximum surface concentration 1.5%.

The temporal prediction error, $\delta_c(t_k)$, of prediction from the result obtained from the traditional method is calculated according to Equation (26). It decreases from 0.041 on the 20th year to 0.015 on the 43rd year, and then continuously increases to 0.152 on the 100th year, see Figure 7. Considering the complexity of the boundary condition, the prediction is reasonably accurate, and the influence of factors in the analysis will be investigated to improve the prediction accuracy.

The computational efficiency of the method is evaluated. In terms of data compression, the size of the essential information is reduced by 99.72%. In terms of memory

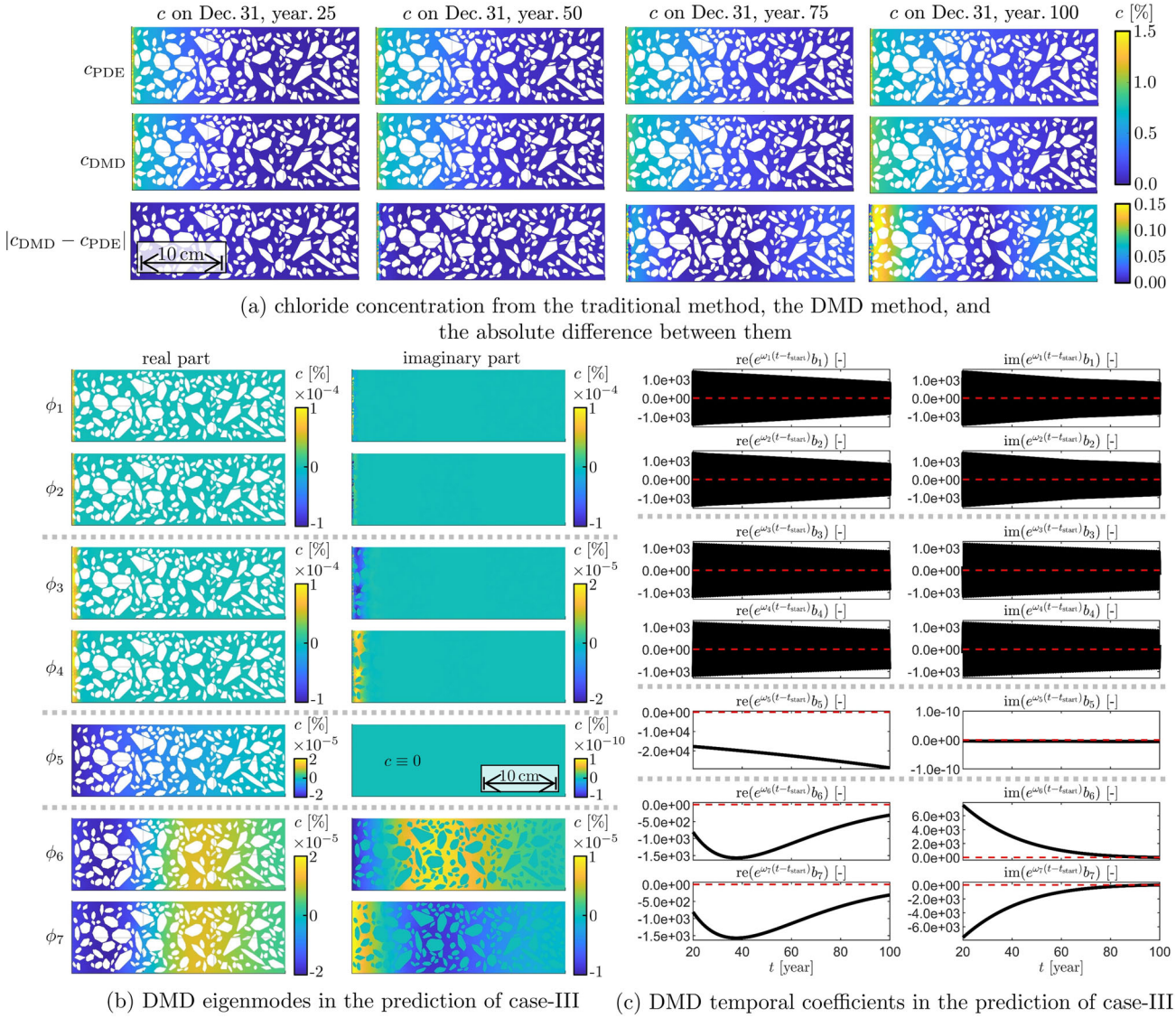

(a) chloride concentration from the traditional method, the DMD method, and the absolute difference between them

(b) DMD eigenmodes in the prediction of case-III

(c) DMD temporal coefficients in the prediction of case-III

FIGURE 6 Analysis of Case-III: (a) comparison of concentration distribution between the data and the prediction, (b) DMD eigenmodes, and (c) DMD temporal coefficients.

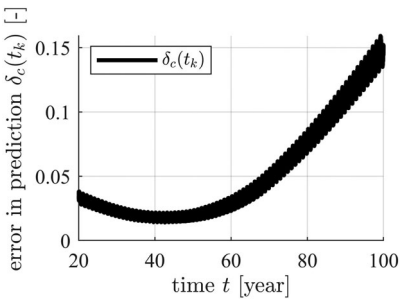

FIGURE 7 Prediction error $\delta_c(t_k)$ over time in Case-III.

usage, the PDE-based solution uses 1640 MB of memory, while the DMD-based solution uses 14240 MB. In terms of time consumption, the PDE-based solution takes 1595 s, whereas the DMD-based solution requires only 3 s, achieving a 99.8% reduction in computation time.

4 | DISCUSSIONS

4.1 | Effect of time window selection on data input

The time window of input data for all three cases was set from the 20th year to the 100th year. In practical engineering, ion concentration measurements may begin immediately after concrete placement by means of embedded sensors, like anode ladder or array systems (Xiao et al., 2025), or later through destructive testing. Data may be collected over days, months, or years. Variations in the

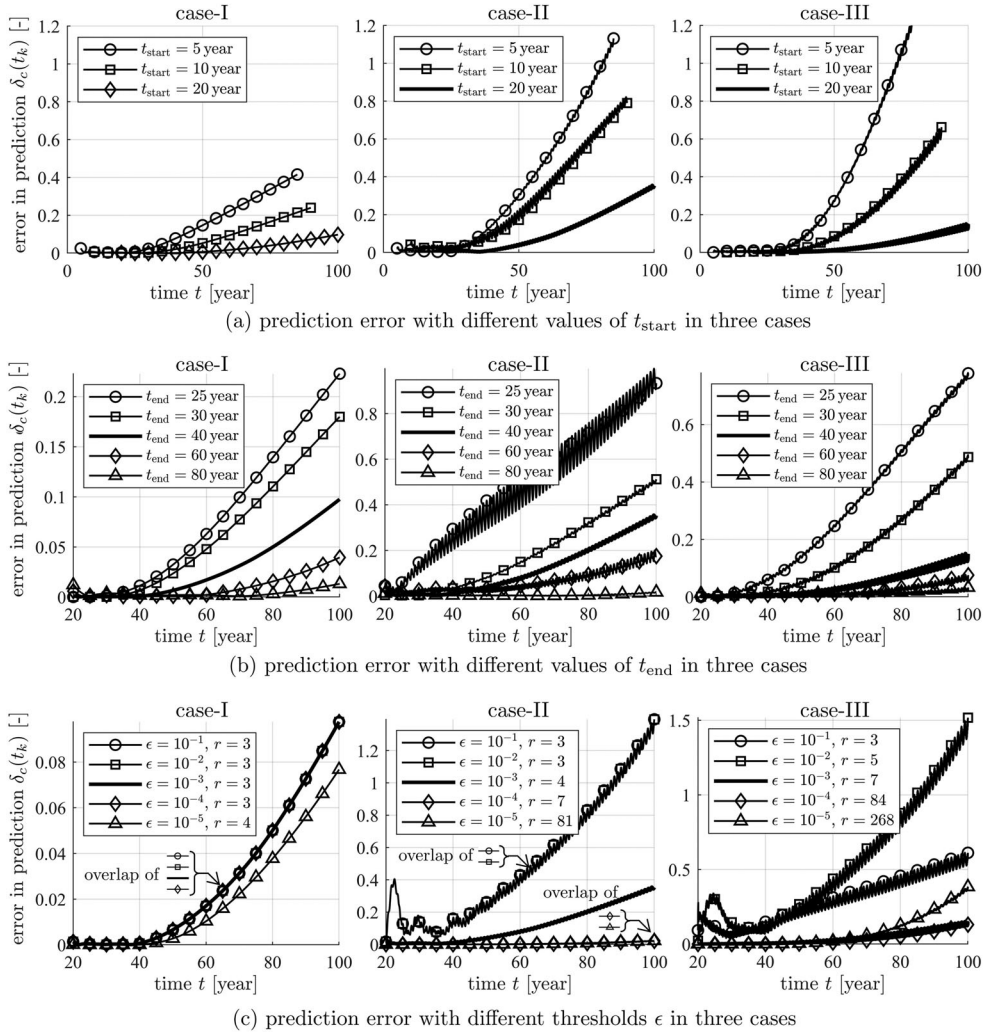

FIGURE 8 Sensitivity analyses of the prediction error for three cases with respect to (a) t_{start}, (b) t_{end}, and (c) the threshold ϵ.

measurement start time and duration change the input data window, affecting both the computational cost of the traditional calculation and SVD steps, as well as the prediction accuracy. To assess this impact, two sensitivity analyses are conducted: one examining the effect of the starting time and the other analyzing the effect of the time window length.

The influence of the start time, t_{start}, is evaluated by repeating all analyses with values of 5 and 10 years while keeping the window length fixed at 20 years. The prediction errors, calculated by Equation (26), exhibit a clear trend that accuracy improves as t_{start} increases, see Figure 8a. Data collected after the concrete has undergone long-term chloride ingress or multiple boundary cycles yield more realistic initial amplitudes and higher prediction accuracy. Thus, input data should preferably come from concrete that has already experienced significant chloride exposure.

The influence of the length of the time window of the input data is explored by repeating the analyses of three cases with its value changed from 20 to 5, 10, 40, and 60 years. The error of prediction is quantified according to Equation (26) for all the analyses, see Figure 8b. The predictive accuracy improves with longer data windows. When the input duration is increased to 40 or 60 years, the final prediction error is reduced to around 0.1 and 0.02, respectively, across all three cases. This demonstrates that incorporating a longer observation period captures more dynamic features of chloride ingress, resulting in better-informed models. Comparing the three simulations under the same accuracy requirement, the more complex the case, the more data it requires. For example, to ensure $\delta_c(t_k) \leq 0.1$, Case-I needs data covering 40 years, while Cases II and III require data spanning over 60 years. Therefore, the input window length should be optimized based on the desired prediction accuracy and the available computational or experimental resources. Notably, extending the input time window does not significantly increase the truncated rank: in Case-I, r remains 3; in Case-II, it rises from 3 to 5; and in Case-III, it remains 7. This indicates

that enriching the input data improves the accuracy of the DMD modes without necessarily increasing the truncated rank or computational cost.

In summary, prediction accuracy strongly depends on the input data. Later starting times and longer observation periods yield more reliable predictions. It is recommended to collect as much data as feasible from concrete that has already experienced long-term chloride ingress and sufficient boundary cycles.

4.2 | Effect of energy loss threshold ϵ in determining truncation rank

The energy loss threshold ϵ in DMD analyses determines how many dominant modes are retained in the reduced model. A smaller ϵ preserves more modes (higher truncated rank r) and thus captures more physical dynamics of chloride transport, whereas a larger ϵ filters out weaker modes, reducing computational cost but possibly oversimplifying the system. To examine this effect, a sensitivity analysis was performed by varying ϵ from 10^{-1} to 10^{-5} in the three studied cases, while keeping other settings, such as the data input window and the prediction period, identical to those in Section 3. The resulting truncated ranks and prediction errors are evaluated using Equations (7) and (26), see Figure 8c.

In Case-I, lowering ϵ from 10^{-1} to 10^{-5} increased the truncated rank from 3 to 4 and reduced the prediction error from 0.0976 to 0.0767. In Case-II, r rose sharply from 3 to 81, decreasing the prediction error at the 100th year from 1.390 to 0.0224. In Case III, the truncated rank eventually reached 268; the error first increased from 0.612 ($r = 3$) to 1.517 ($r = 5$), then dropped to 0.130 ($r = 84$), and finally rose again to 0.383 ($r = 268$). This non-monotonic trend indicates that excessive mode retention may introduce overfitting or numerical instability. Overall, while a smaller ϵ generally improves accuracy by retaining more physical information, overly small values can inflate computational cost and reduce robustness. Hence, selecting an appropriate ϵ requires balancing accuracy and efficiency.

4.3 | Effect of linear transformations on boundary conditions

The influence of the linear transformation of fluctuations in boundary conditions on the performance of the method is investigated herein. It corresponds to the scenario in practice, where environmental exposures across different parts of a concrete structure often share similar temporal patterns but differ in magnitude. To assess this effect, an additional analysis, denoted as Case-IV, is conducted based on Case-II, with the amplitude of the annual fluctuation doubled, see Figure 9. The surface concentration in case IV is expressed as

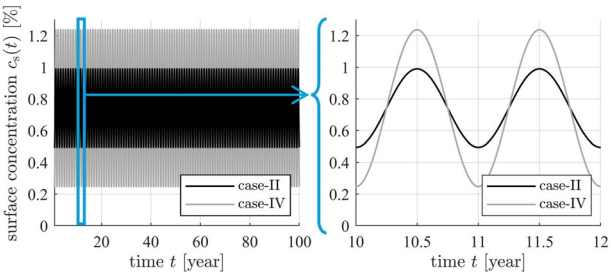

FIGURE 9 Evolution of surface chloride concentration, $c_{\text{surf}}(t)$, in the boundary condition of Case-IV.

$$c_{\text{surf,IV}}(t) = \frac{0.435\% - 0.29\% \cos\left(\frac{2\pi t}{\Delta t_{\text{year}}}\right)}{1 - f_{\text{agg}}^{\text{con}}} \tag{31}$$

Case-IV is analyzed following the same procedure as before. The truncated rank r remains 4, as determined by Equation (7). The corresponding DMD eigenmodes are shown in Figure 10a, with the initial amplitude vector $\boldsymbol{b}$ and the matrix of growth ratios $\boldsymbol{\Omega}$ defined as

$$\boldsymbol{b} = \begin{pmatrix} -2.19 + 0.807i \\ -2.19 - 0.807i \\ -9.97 + 13.5i \\ -9.97 - 13.5i \end{pmatrix} \times 10^3,\ \boldsymbol{b} \in \mathbb{R}^{4\times 1} \tag{32}$$

$$\boldsymbol{\Omega} = \text{diag}\begin{pmatrix} 524i \\ -524i \\ -0.600 + 1.30i \\ -0.600 - 1.30i \end{pmatrix} \times 10^{-3},\ \boldsymbol{\Omega} \in \mathbb{R}^{4\times 4} \tag{33}$$

The temporal coefficients, $e^{\boldsymbol{\Omega}(t-t_{\text{start}})}\boldsymbol{b}$, are obtained using Equation (17) and illustrated in Figure 10b.

The temporal prediction error in Case-IV, see Figure 11, closely matches that of Case-II, see Figure 5. The DMD eigenmodes $\boldsymbol{\Phi}$ in case IV are sign-inverted relative to those in case-II, and the first two elements of $\boldsymbol{b}$, corresponding to oscillating modes, are approximately doubled, reflecting the increased boundary amplitude. Reversing the signs of both $\boldsymbol{\Phi}$ and $\boldsymbol{b}$ leaves the prediction unchanged but clarifies their correspondence to Case-II. The difference between the flipped eigenmodes in Case-IV and the original ones in Case-II, computed analogously to Equation (26), is below 0.05.

These findings indicate that scaling the amplitude of the boundary fluctuation leads to a proportional scaling of the oscillatory components in $\boldsymbol{b}$, while the modal structure $\boldsymbol{\Phi}$ and dynamic characteristics $\boldsymbol{\Omega}$ remain unchanged. Physically, this demonstrates the linear response of the sys-

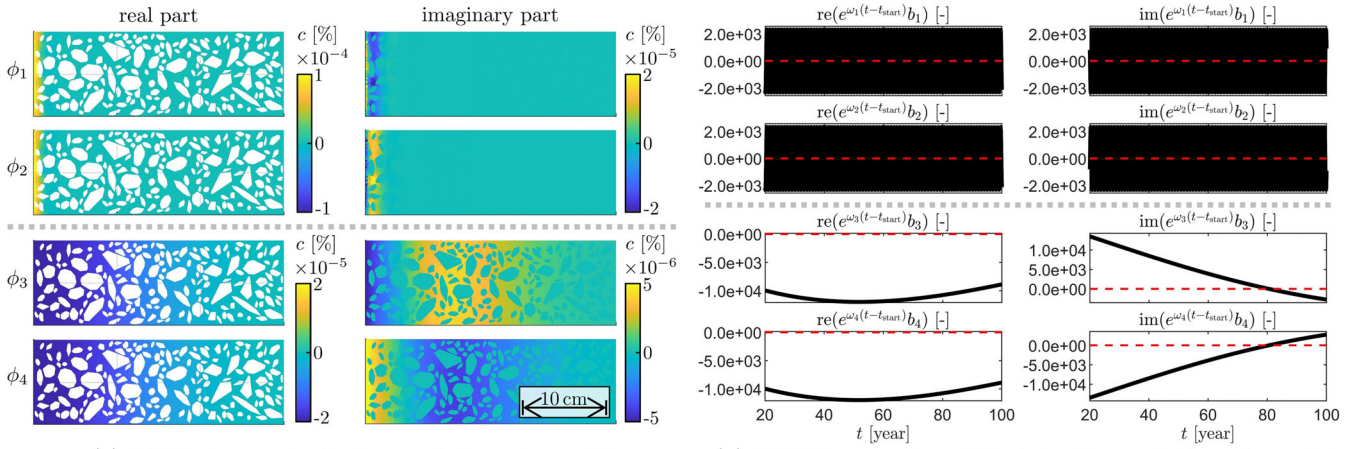

(a) DMD eigenmodes in the prediction of case-IV (b) DMD temporal coefficients in the prediction of case-IV

FIGURE 10 Analysis of Case-IV: (a) DMD eigenmodes and (b) DMD temporal coefficients.

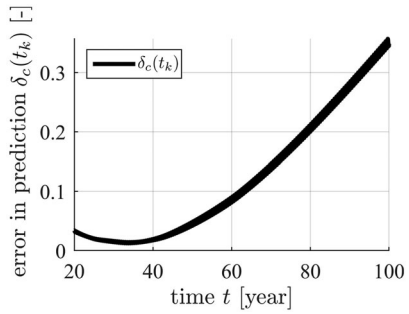

FIGURE 11 Prediction error $\delta_c(t_k)$ over time in Case-IV.

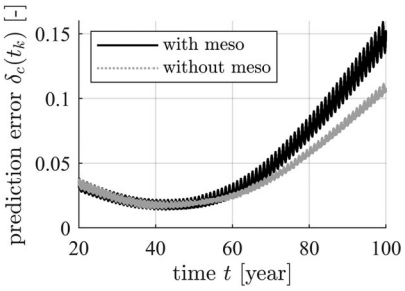

FIGURE 12 Prediction error $\delta_c(t_k)$ with or without concrete heterogeneity considered.

tem: Boundary amplitude variations affect the intensity of modal excitation but not the intrinsic temporal dynamics captured by $\boldsymbol{\Omega}$.

4.4 | Effect of concrete heterogeneity

The influence of concrete heterogeneity on prediction accuracy was examined by an additional analysis based on Case-III. The concrete is treated as a homogeneous phase herein. The prediction error reached 0.11 at the 100th year, lower than 0.15 in Case-III, see Figure 12. This comparison indicates that the method achieves higher accuracy for homogeneous concrete and, equivalently, requires less data to reach the same accuracy as in heterogeneous cases.

4.5 | Effect of noise in the input data

The analyses above are based on ideal numerical data, whereas real measurements inevitably contain noise from various sources. The robustness of a data-driven method against the complexity in data is essential for its application (Rafiei & Adeli, 2017). To assess it, a sensitivity analysis was performed by introducing Gaussian noise into the input data of Case-III. This simplified noise model represents common signal transfer errors, while more complex random-field noise from measurements is disregarded here.

Numerically, each concentration value in the spatial–temporal input matrix was multiplied by a random coefficient sampled from a normal distribution with a mean of one and a standard deviation of σ_{noise}, representing the noise level. The evolution of the prediction error $\delta_c(t_k)$ was evaluated with σ_{noise} of 0.5%, 1%, and 2%. The prediction remained stable for σ_{noise} below 2%, beyond which the error increased by approximately fourfold, see Figure 13. These results indicate that the prediction is robust to low-level noise, though the effects of other noise types warrant further study.

4.6 | Approximate analytical model associated with mode merging

The analyses presented thus far demonstrate the data-driven method for predicting the evolution of chloride concentration distributions in concrete, even under com-

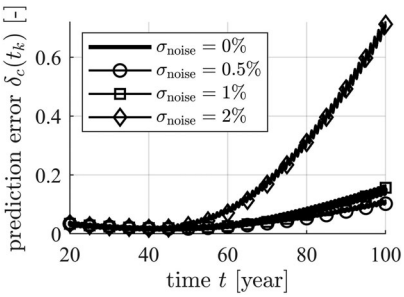

FIGURE 13 Prediction error $\delta_c(t_k)$ with different noise levels.

plex boundary conditions. However, calculations involving large-scale complex vectors are difficult to interpret, verify, and reproduce, particularly for engineers unfamiliar with the DMD method, thereby limiting their practicality in engineering applications. To address this, an analytical model is developed herein to predict the evolution of the concentration profile, $c_d(d,t)$, using a limited number of real-valued variables. For simple boundary conditions with constant surface concentration, such as in Case-I, the chloride profile is well described by the Gauss error function (Collepardi et al., 1972). However, extending this to more complex scenarios, such as Case-II and Case-III, remains challenging. Here, Case-III is selected as an example for constructing such an analytical model. Since the DMD result is already expressed as a sum of eigenmodes multiplied by their respective temporal coefficients, the goal is to approximate the spatial distribution of each eigenmode using explicit functions of depth. In addition, similarities between eigenmodes and their temporal coefficients are used to merge symmetric mode pairs for simplification.

To construct an approximate analytical model for Case-III, the profile $c_{d,\phi_s}(d)$ of concentrations over depth in the DMD eigenmode ϕ_s are extracted first in analogous to $c_{\mathrm{DMD},d}$ in Equation (24). The real and imaginary parts of it is denoted as $c_{d,\phi_s,\mathrm{re}}(d)$ and $c_{d,\phi_s,\mathrm{im}}(d)$, respectively. Each of the seven DMD eigenmodes in case-III thus yields a pair of curves for the real and imaginary parts, see Figure 14a,b. These curves exhibit damped oscillatory behavior along the depth direction. Therefore, they are fitted by a unified function in the form of the product of an exponential function and a sine function:

$$c_{d,\phi_s}(d) = e^{\alpha_1 d+\alpha_2}\sin(\alpha_3 d+\alpha_4) \tag{34}$$

where α_1–α_4 are regression parameters with values regressed with the corresponding R^2 values confirming high fitting quality, see Table 1 as well as Figure 14c,d. These fitted functions render proposing an analytical model possible. The evolution of chloride profile,

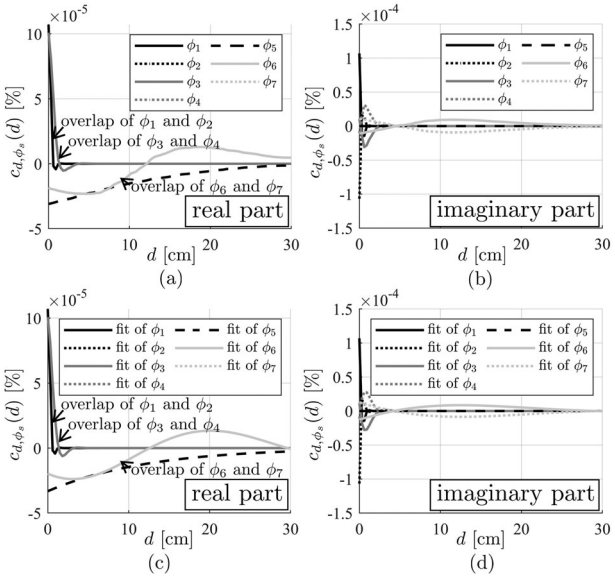

FIGURE 14 Profiles of chloride concentration in DMD modes over depth: (a) real part and (b) imaginary part; and corresponding fitting of profiles: (c) real part and (d) imaginary part.

TABLE 1 Regressed parameter of function fitting the eigenmodes of Case-III.

	Real part				
Eigenmode	α_1	α_2	α_3	α_4	R^2
ϕ_1	−433.5	−2.0	453.5	0.5	1.0000
ϕ_2	−433.5	−2.0	453.5	0.5	1.0000
ϕ_3	−150.4	−2.4	169.0	0.9	0.9993
ϕ_4	−150.4	−2.4	169.0	0.9	0.9993
ϕ_5	−10.0	0.0	0.0	0.0	0.9867
ϕ_6	−3.3	−4.0	18.6	4.0	0.9781
ϕ_7	−3.3	−4.0	18.6	4.0	0.9781
	Imaginary part				
Eigenmode	α_1	α_2	α_3	α_4	R^2
ϕ_1	−376.6	−2.4	415.8	2.2	1.0000
ϕ_2	−378.0	−2.4	413.1	5.3	1.0000
ϕ_3	−120.5	−2.8	132.3	3.0	0.9904
ϕ_4	−120.2	−2.8	132.3	6.2	0.9904
ϕ_5	0.0	$-\infty$	0.0	0.0	–
ϕ_6	−7.4	−4.1	12.7	5.8	0.9788
ϕ_7	−7.3	−4.1	12.7	2.6	0.9788

$c_{\mathrm{DMD},d}(d,t)$, is predicted following:

$$c_{\mathrm{DMD},d}(d,t) = \sum_{s=1}^{r}\left[c_{d,\phi_s,\mathrm{re}}(d) + ic_{d,\phi_s,\mathrm{im}}(d)\right] e^{\omega_s(t-t_{\mathrm{start}})} b_s \tag{35}$$

Inserting the parameters of Case-III, see Equations (29) and (30) and Table 1, into Equation (35) yields the predicted profiles of chloride concentration over time. To investi-

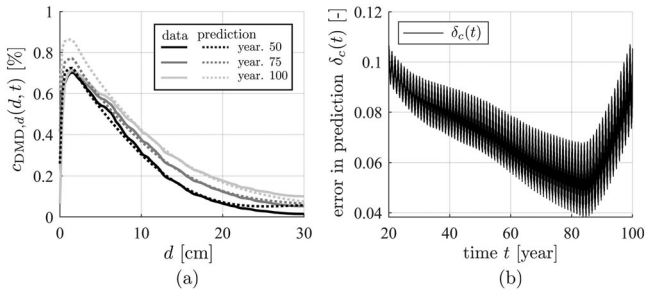

FIGURE 15 (a) Prediction of chloride ingress with the analytical model, and (b) its error compared with the data from the traditional computation.

gate the accuracy of the prediction, the corresponding profile is extracted from the original data from the traditional approach and is denoted as $c_{\mathrm{PDE},d}(d,t)$. Starting from the 20th, the curves of $c_{\mathrm{PDE},d}(d,t)$ and $c_{\mathrm{DMD},d}(d,t)$ almost overlap until the 60th year, see Figure 15a. After year 60, slight overestimation is observed near the surface, up to 20%, while predictions remain accurate at greater depths. The temporal prediction error $\delta_c(t)$ between $c_{\mathrm{PDE},d}(d,t)$ and $c_{\mathrm{DMD},d}(d,t)$ is evaluated in analogy with Equation (26):

$$\delta_c(t) = \frac{\int_0^{d_{\max}} \left| c_{\mathrm{DMD},d}(d,t) - c_{\mathrm{PDE},d}(d,t) \right| \mathrm{d}d}{\int_0^{d_{\max}} \left| c_{\mathrm{PDE},d}(d,t) \right| \mathrm{d}d} \tag{36}$$

where $d_{\max}$ is equal to 30 cm. The error remains below 0.11 for the entire prediction period from the 20th year to the 100th year, see Figure 15b.

Emerging modes provide the possibility of further simplifying the current analytical model. Currently, the eigenmodes and the temporal coefficients could be classified into two types: (i) purely real modes with both the spatial eigenmode and temporal coefficient all being purely real, like the fifth mode in Case-III, and (ii) complex conjugate pairs that share identical real parts and symmetric imaginary parts in both spatial eigenmodes and temporal coefficients, like the first and second, the third and the fourth, and the sixth and seventh modes in Case-III. If the sth mode belongs to the first type, its contribution to $c_d(d,t)$, $c_{d,j}(d,t)$, is expressed as

$$c_{d,s}(d,t) = c_{d,\phi_s}(d)\, e^{\omega_s (t-t_{\mathrm{start}})} b_s \tag{37}$$

with all variables purely real. If the sth and $(s+1)$th modes belongs to the second type, forming a complex conjugate pair, their contribution to $c_d(d,t)$, $c_{d,s\&(s+1)}(d,t)$, is expressed as

$$\begin{aligned} c_{d,s\&(s+1)}(d,t) &= c_{d,\phi_s}(d)\, e^{\omega_s (t-t_{\mathrm{start}})} b_s \\ &+ c_{d,\phi_{s+1}}(d)\, e^{\omega_{s+1} (t-t_{\mathrm{start}})} b_{s+1} \end{aligned} \tag{38}$$

Denoting the real and imaginary parts of variables by appending "re" and "im" on their subscript, the complex conjugate relation between the sth and $(s+1)$th modes are expressed as

$$\begin{aligned} c_{d,\phi_{s+1},\mathrm{re}}(d) &= \; c_{d,\phi_s,\mathrm{re}}(d), \\ c_{d,\phi_{s+1},\mathrm{im}}(d) &= -c_{d,\phi_s,\mathrm{im}}(d) \end{aligned} \tag{39}$$

$$\omega_{s+1,\mathrm{re}} = \omega_{s,\mathrm{re}}, \quad \omega_{s+1,\mathrm{im}} = -\omega_{s,\mathrm{im}} \tag{40}$$

$$b_{s+1,\mathrm{re}} = b_{s,\mathrm{re}}, \quad b_{s+1,\mathrm{im}} = -b_{s,\mathrm{im}} \tag{41}$$

Inserting Equations (39)–(41) into Equation (38) yields its simplification as

$$\begin{aligned} &c_{j\&(j+1)}(d,t) \\ &= e^{\omega_{s,\mathrm{re}}(t-t_{\mathrm{start}})} \left[c_{d,\phi_s,\mathrm{re}}(d)\, b'_{s,\mathrm{re}} - c_{d,\phi_s,\mathrm{im}}(d)\, b'_{s,\mathrm{im}} \right] \end{aligned} \tag{42}$$

where $(b'_{s,\mathrm{re}}, b'_{s,\mathrm{im}})^{\mathrm{T}}$ is equal to $(b_{s,\mathrm{re}}, b_{s,\mathrm{im}})^{\mathrm{T}}$ after time-dependent rotation with the frequency of these modes:

$$\begin{bmatrix} b'_{s,\mathrm{re}} \\ b'_{s,\mathrm{im}} \end{bmatrix} = \begin{bmatrix} \cos(\omega_{s,\mathrm{im}}(t')) & -\sin(\omega_{s,\mathrm{im}}(t')) \\ \sin(\omega_{s,\mathrm{im}}(t')) & \cos(\omega_{s,\mathrm{im}}(t')) \end{bmatrix} \begin{bmatrix} b_{s,\mathrm{re}} \\ b_{s,\mathrm{im}} \end{bmatrix} \tag{43}$$

where t' denotes $t - t_{\mathrm{start}}$. This transformation eliminates the need for complex calculation, allowing all components of $c_d(d,t)$ to be computed using real-valued functions, making the analytical model more intuitive and practical for engineering applications.

The derivation of the analytical model in Case III can be generalized to any scenario that can be predicted by the proposed method. Once the eigenmodes and their temporal coefficients are obtained, the prediction can be reformulated as a real-valued analytical model with only a few variables, achieved here for the first time.

4.7 | Physical self-consistency of the method with respect to the divergence theorem

Physical self-consistency of the proposed DMD-based method is evaluated herein with respect to the divergence theorem. Since this method provides the prediction of the spatio-temporal evolution of ion concentration purely from data, there is a risk of violating fundamental physical laws, which would limit its engineering applicability. For two-dimensional analysis of chloride ingress in concrete, the divergence theorem (Kreyszig, 2011), also known

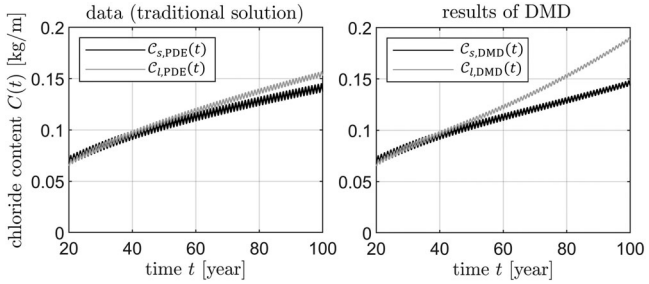

FIGURE 16 Physical self-consistency of the predicted chloride ingress in Case-III with respect to the divergence theorem: (a) the data obtained from the traditional solution and (b) the results obtained from the proposed method based on DMD.

as Gauss–Ostrogradsky theorem, requires

$$\iint_{\Omega_s} \nabla \cdot \boldsymbol{J}(x,t)\ \mathrm{d}s \equiv \oint_{\Omega_l} \boldsymbol{J}(x,t) \cdot \boldsymbol{n}\ \mathrm{d}l \tag{44}$$

where $\nabla \cdot \boldsymbol{J} = \nabla \cdot \boldsymbol{J}$, and ∇ denotes the vector differential (nabla) operator, $\boldsymbol{J}(x,t)$ is the chloride ion flux, and $\boldsymbol{n}$ is the outward-pointing unit normal to the boundary. The left side of Equation (44) is an area integral over the model's area Ω_s, and the right side is a line integral over its boundary Ω_l. Inserting the mass conservation relation $\frac{\partial c(x,t)}{\partial t} = -\nabla \cdot \boldsymbol{J}(x,t)$ and Fick's first law $\boldsymbol{J}(x,t) = -D_{\mathrm{mor}} \nabla c(x,t)$ (Dhir et al., 1998) into the left- and right-hand sides of Equation (44) yields

$$\frac{\partial}{\partial t} \iint_{\Omega_s} c(x,t)\ \mathrm{d}s = \oint_{\Omega_l} D_{\mathrm{mor}} \nabla c(x,t) \cdot \boldsymbol{n}\ \mathrm{d}l \tag{45}$$

Integrating both sides of Equation (45) from t_{start} gives the ion content $C(t)$ as a criterion for self-consistency

$$\begin{aligned} \iint_{\Omega_s} c(x,t)\ \mathrm{d}s &= C(t_{\mathrm{start}}) \\ &+ \int_{t_{\mathrm{start}}}^{t} \left[\oint_{\Omega_l} D_{\mathrm{mor}} \nabla c(x,t) \cdot \boldsymbol{n}\ \mathrm{d}l \right] \mathrm{d}t \end{aligned} \tag{46}$$

The analysis in Case-III is examined herein according to Equation (46) with the area- and boundary-integrated ion contents denoted as $C_s(t)$ and $C_l(t)$, respectively. For the data from the traditional solution, the predicted evolution of the ion content in the model, $C_{s,\mathrm{PDE}}(t)$, is close to the one calculated from the flux on the boundary, $C_{l,\mathrm{PDE}}(t)$, see Figure 16, and the maximum deviation between them is 10.3%. This discrepancy mainly arises from numerical approximation in evaluating the integrals over discretized spatial and temporal snapshots. For the proposed DMD-based method, the area integral for ion content, $C_{s,\mathrm{DMD}}(t)$, is close to the result from the data, $C_{s,\mathrm{PDE}}(t)$, which is consistent with the prediction accuracy shown in Figure 7. However, the ion content calculated from the flux on the boundary, $C_{l,\mathrm{DMD}}(t)$, increases much quicker than $C_{s,\mathrm{DMD}}(t)$, indicating a substantial error in predicting the ion concentration near to the left boundary. The maximum deviation between the two approaches reaches 23.8%, which is higher than that of the PDE-based solution. Notably, part of this deviation arises from input data errors, which could be reduced by shortening time steps and tightening error tolerances in the preparing the data in the traditional solution.

To satisfy the divergence theorem in prediction, mass conservation between the model and its environment must be ensured. For this purpose, the concentration vectors are reorganized for convenient quantification of ion content and denoted as $\boldsymbol{c}_k{}^*$, containing concentrations interpolated onto M^* uniformly distributed spatial points in the model. The ion content of the model is given by $(S_{\mathrm{mod}}/M^*)(\mathbf{1}^{\mathrm{T}}\boldsymbol{c}_k{}^*)$, where S_{mod} denotes the model area. The relative change of ion content in the environment is expressed as $-\nabla\bar{\boldsymbol{c}}_k{}^* D_{\mathrm{mor}} L_{\mathrm{edge}}$, where $\nabla\bar{c}_k{}^*$ is the average concentration gradient along the open boundary of length L_{edge}. By appending $\boldsymbol{c}_k{}*$ with this environmental term scaled as $-\nabla\bar{\boldsymbol{c}}_k^* D_{\mathrm{mor}} L_{\mathrm{edge}} M^*/S_{\mathrm{mod}}$, a new vector $\boldsymbol{c}_k{}**$ is obtained. For the combined system of the model and environment, mass conservation requires

$$\frac{S_{\mathrm{mod}}}{M^*}\left(\mathbf{1}^{\mathrm{T}}\boldsymbol{A}\boldsymbol{c}_k{}^{**}\right) = \frac{S_{\mathrm{mod}}}{M^*}\left(\mathbf{1}^{\mathrm{T}}\boldsymbol{c}_k{}^{**}\right) \tag{47}$$

which simplifies to $\mathbf{1}^{\mathrm{T}}\boldsymbol{A} = \mathbf{1}^{\mathrm{T}}$. It enforces the column sum of $\boldsymbol{A}$ equal one, which is the sought constrained condition for ensuring the physical self-consistence of DMD in predicting chloride ingress.

5 | CONCLUSION

A novel data-driven approach was developed to predict chloride ingress in concrete. Based on the analyses, the following conclusions regarding the contributions to the DMD method, the performance in prediction, and the developed analytical model are drawn:

1. DMD is extended to a highly heterogeneous, non-periodic system, chloride ingress in concrete, with complex spatio-temporal evolution rarely addressed previously. A real-valued analytical model is derived from the DMD results to predict chloride ingress in any scenario where the method applies. Prediction deviations in these cases are larger than in classic DMD applications, such as fluid flows or acoustics, highlighting the challenges of complex concrete scenarios.

Sensitivity analyses show that errors increase with limited input data, over-truncated ranks, or higher noise levels, which may ultimately lead to prediction failure. These findings also point to directions for further improvement of the DMD method.

2. The performance of the method has been demonstrated in predicting chloride ingress under constant, annual cyclic, and multi-frequency cyclic boundary conditions, with concrete heterogeneity explicitly considered. For 60-year predictions using 20-year data, the error remains below 0.1, the data storage is compressed by over 99% and computational time-consumption is reduced by more than 91%.
3. A real-valued analytical model is derived to predict chloride ingress, which is, for the first time, in any scenario where the method applies. This model expresses the chloride profile as a sum of spatial modes multiplied by temporal coefficients, avoiding high-dimensional computations. Thus, it is interpretable and practical for engineering applications.

With the increasing use of embedded sensors in concrete bridges, long-term chloride data can now be continuously collected. The proposed method leverages these histories to forecast chloride ingress, supporting the estimation of corrosion progression, residual capacity, and service life. The resulting real-valued analytical models are easily integrated into performance-based design, reliability assessment, and maintenance planning, making the approach both scientifically innovative and practically applicable for design codes and structural monitoring. The models and data used in this study will be made publicly available on GitHub. This will facilitate transparency and support further research based on the present work.

NOMENCLATURE

$\boldsymbol{x}$, $\boldsymbol{X}$	State vector and matrix
$\boldsymbol{A}$	Linear operator
$\tilde{\boldsymbol{A}}$	Order-reduced operator
c, $\boldsymbol{c}$, $\boldsymbol{C}$	Concentration value, vector, and matrix
C	Chloride content
c_{surf}	Surface concentration
D	Diffusion coefficient
$\boldsymbol{J}$	Chloride ion flux
r	Truncated rank
t	Time
$\boldsymbol{U}$, $\boldsymbol{\Sigma}$, $\boldsymbol{V}$	SVD components
$\boldsymbol{W}$, $\boldsymbol{\Lambda}$	Eigenvector and eigenvalue
ϵ	Energy loss threshold
δ_c	Temporal prediction error
$\boldsymbol{\Phi}$, $\boldsymbol{b}$	DMD eigenmode and initial amplitude
$\boldsymbol{\Omega}$	Eigenvalue $\ln(\boldsymbol{\Lambda})/\Delta t$

ACKNOWLEDGMENTS

This project has received funding from the European Union's Horizon Europe Research and Innovation Programme under the European Research Council (ERC) Synergy Grant Agreement No. 101167045 (FatResCon). The second author additionally received support from the Czech Science Foundation under grant no. GA24-10892S.

Open access publishing facilitated by Vysoke uceni technicke v Brne, as part of the Wiley - CzechELib agreement.

REFERENCES

Ababneh, A., Benboudjema, F., & Xi, Y. (2003). Chloride penetration in nonsaturated concrete. *Journal of Materials in Civil Engineering*, *15*(2), 183–191. https://doi.org/10.1061/(ASCE)0899-1561(2003)15:2(183)

Alam, K. M. R., Siddique, N., & Adeli, H. (2020). A dynamic ensemble learning algorithm for neural networks. *Neural Computing and Applications*, *32*(12), 8675–8690. https://doi.org/10.1007/s00521-019-04359-7

Angle, J. P., Wang, Z., Dames, C., & Mecartney, M. L. (2013). Comparison of two-phase thermal conductivity models with experiments on dilute ceramic composites. *Journal of the American Ceramic Society*, *96*(9), 2935–2942. https://doi.org/10.1111/jace.12488

Bai, Z., Kaiser, E., Proctor, J. L., Kutz, J. N., & Brunton, S. L. (2020). Dynamic mode decomposition for compressive system identification. *AIAA Journal*, *58*(2), 561–574. https://doi.org/10.2514/1.j057870

Bastidas-Arteaga, E., Chateauneuf, A., Sánchez-Silva, M., Bressolette, P., & Schoefs, F. (2011). A comprehensive probabilistic model of chloride ingress in unsaturated concrete. *Engineering Structures*, *33*(3), 720–730. https://doi.org/10.1016/j.engstruct.2010.11.008

Bažant, Z. P. (1979a). Physical model for steel corrosion in concrete sea structures—Application. *Journal of the Structural Division*, *105*(6), 1155–1166. https://doi.org/10.1061/JSDEAG.0005169

Bažant, Z. P. (1979b). Physical model for steel corrosion in concrete sea structures—Theory. *Journal of the Structural Division*, *105*(6), 1137–1153. https://doi.org/10.1061/JSDEAG.0005168

Biondini, F., Bontempi, F., Frangopol, D., Asce, F., & Malerba, P. (2004). Cellular automata approach to durability analysis of concrete structures in aggressive environments. *Journal of Structural Engineering*, *130*(11). https://doi.org/10.1061/(ASCE)0733-9445(2004)130:11(1724)

Cai, R., Han, T., Liao, W., Huang, J., Li, D., Kumar, A., & Ma, H. (2020). Prediction of surface chloride concentration of marine concrete using ensemble machine learning. *Cement and Concrete Research*, *136*, 106164. https://doi.org/10.1016/j.cemconres.2020.106164

Collepardi, M., Marcialis, A., & Turriziani, R. (1972). Penetration of chloride ions into cement pastes and concretes. *Journal of the American Ceramic Society*, *55*(10), 534–535. https://doi.org/10.1111/j.1151-2916.1972.tb13424.x

Cusson, D., Lounis, Z., & Daigle, L. (2011). Durability monitoring for improved service life predictions of concrete bridge decks

in corrosive environments. *Computer-Aided Civil and Infrastructure Engineering*, *26*(7), 524–541. https://doi.org/10.1111/j.1467-8667.2010.00710.x

Dhir, R. K., Jones, M. R., & Ng, S. L. D. (1998). Prediction of total chloride content profile and concentration/time-dependent diffusion coefficients for concrete. *Magazine of Concrete Research*, *50*(1), 37–48. https://doi.org/10.1680/macr.1998.50.1.37

Glass, G. K., & Buenfeld, N. R. (2000). The influence of chloride binding on the chloride induced corrosion risk in reinforced concrete. *Corrosion Science*, *42*(2), 329–344. https://doi.org/10.1016/s0010-938x(99)00083-9

Jensen, O. M., Hansen, P. F., Coats, A. M., & Glasser, F. P. (1999). Chloride ingress in cement paste and mortar. *Cement and Concrete Research*, *29*(9), 1497–1504. https://doi.org/10.1016/s0008-8846(99)00131-3

Kim, J., McCarter, W. J., Suryanto, B., Nanukuttan, S., Basheer, P. A. M., & Chrisp, T. M. (2016). Chloride ingress into marine exposed concrete: A comparison of empirical-and physically-based models. *Cement and Concrete Composites*, *72*, 133–145. https://doi.org/10.1016/j.cemconcomp.2016.06.002

Koch, G., Varney, J., Thompson, N., Moghissi, O., Gould, M., & Payer, J. (2016). *International measures of prevention, application, and economics of corrosion technologies study*. Nace International.

Kreyszig, E. (2011). *Advanced engineering mathematics* (10th ed.). Wiley & Sons.

Kuntal, V. S., Jiradilok, P., Bolander, J. E., & Nagai, K. (2021). Estimation of internal corrosion degree from observed surface cracking of concrete using mesoscale simulation with model predictive control. *Computer-Aided Civil and Infrastructure Engineering*, *36*(5), 544–559. https://doi.org/10.1111/mice.12620

Liu, Q., Li, L., Easterbrook, D., & Yang, J. (2012). Multi-phase modelling of ionic transport in concrete when subjected to an externally applied electric field. *Engineering Structures*, *42*, 201–213. https://doi.org/10.1016/j.engstruct.2012.04.021

Mohan, N., Soman, K. P., & Kumar, S. S. (2018). A data-driven strategy for short-term electric load forecasting using dynamic mode decomposition model. *Applied Energy*, *232*, 229–244. https://doi.org/10.1016/j.apenergy.2018.09.190

Niklasson, G. A., Granqvist, C. G., & Hunderi, O. (1981). Effective medium models for the optical properties of inhomogeneous materials. *Applied Optics*, *20*(1), 26–30. https://doi.org/10.1364/ao.20.000026

Nilsson, L.-O. (2022). Models for chloride ingress—An overview. In E. Koenders, K.-I. Imamoto, & A. Soive (Eds.). *Benchmarking chloride ingress models on real-life case studies—Marine submerged and road sprayed concrete structures: State-of-the-art report of the RILEM TC 270-CIM*. (pp. 7–23). Springer. https://doi.org/10.1504/IJMIC.2009.027065

Papadakis, V. G. (2000). Effect of supplementary cementing materials on concrete resistance against carbonation and chloride ingress. *Cement and Concrete Research*, *30*(2), 291–299. https://doi.org/10.1016/S0008-8846(99)00249-5

Pereira, D. R., Piteri, M. A., Souza, A. N., Papa, J. P., & Adeli, H. (2020). FEMa: A finite element machine for fast learning. *Neural Computing and Applications*, *32*(10), 6393–6404. https://doi.org/10.1007/s00521-019-04146-4

Qiu, Q., & Dai, J.-G. (2021). Meso-scale modeling of chloride diffusivity in mortar subjected to corrosion-induced cracking. *Computer-Aided Civil and Infrastructure Engineering*, *36*(5), 602–619. https://doi.org/10.1111/mice.12657

Radlińska, A., McCarthy, L. M., Matzke, J., & Nagel, F. (2014). Synthesis of DOT use of beam end protection for extending the life of bridges. *International Journal of Concrete Structures and Materials*, *8*(3), 185–199. https://doi.org/10.1007/s40069-014-0077-0

Rafiei, M. H., & Adeli, H. (2017). A new neural dynamic classification algorithm. *IEEE Transactions on Neural Networks and Learning Systems*, *28*(12), 3074–3083. https://doi.org/10.1109/TNNLS.2017.2682102

Ruan, X., Li, Y., Jin, Z., Pan, Z., & Yin, Z. (2019). Modeling method of concrete material at mesoscale with refined aggregate shapes based on image recognition. *Construction and Building Materials*, *204*, 562–575. https://doi.org/10.1016/j.conbuildmat.2019.01.157

Šavija, B., Luković, M., & Schlangen, E. (2014). Lattice modeling of rapid chloride migration in concrete. *Cement and Concrete Research*, *61-62*(S61-62), 49–63. https://doi.org/10.1016/j.cemconres.2014.04.004

Šavija, B., Pacheco, J., & Schlangen, E. (2013). Lattice modeling of chloride diffusion in sound and cracked concrete. *Cement and Concrete Composites*, *42*(9), 30–40. https://doi.org/10.1016/J.CEMCONCOMP.2013.05.003

Schmid, P., & Sesterhenn, J. (2008). Dynamic mode decomposition of numerical and experimental data. *Bulletin of the American Physical Society, 61st Annual Meeting of the APS Division of Fluid Dynamics 53*(15).

Schmid, P. J. (2010). Dynamic mode decomposition of numerical and experimental data. *Journal of Fluid Mechanics*, *656*, 5–28. https://doi.org/10.1017/s0022112010001217

Strauss, A., Teply, B., Novák, D., Pukh, R., Bergmeister, K., & Wan-Wendner, R. (2010). Analysis and reliability assessment of chloride deteriorated pre-stressed concrete structures–Part II. *Proceedings of the 8th International Probabilistic Workshop*, Szczecin, Poland.

Tang, L., & Joost, G. (2007). On the mathematics of time-dependent apparent chloride diffusion coefficient in concrete. *Cement and Concrete Research*, *37*(4), 589–595. https://doi.org/10.1016/j.cemconres.2007.01.006

Tong, L., Liu, Q., Xiong, Q., Meng, Z., Amiri, O., & Zhang, M. (2025). Modeling the chloride transport in concrete from microstructure generation to chloride diffusivity prediction. *Computer-Aided Civil and Infrastructure Engineering*, *40*(9), 1129–1149. https://doi.org/10.1111/mice.13331

Torres-Luque, M., Bastidas-Arteaga, E., Schoefs, F., Sánchez-Silva, M., & Osma, J. F. (2014). Non-destructive methods for measuring chloride ingress into concrete: State-of-the-art and future challenges. *Construction and Building Materials*, *68*, 68–81. https://doi.org/10.1016/j.conbuildmat.2014.06.009

Tu, J. H., Rowley, C. W., Luchtenburg, D. M., Brunton, S. L., & Kutz, J. N. (2014). On dynamic mode decomposition: Theory and applications. *Journal of Computational Dynamics*, *1*(2), 391–421. https://doi.org/10.3934/jcd.2014.1.391

Viguerie, A., Barros, G. F., Grave, M., Reali, A., & Coutinho, A. L. G. A. (2022). Coupled and uncoupled dynamic mode decomposition in multi-compartmental systems with applications to epidemiological and additive manufacturing problems. *Computer Methods in Applied Mechanics and Engineering*, *391*, 114600. https://doi.org/10.1016/j.cma.2022.114600

Xiao, T., Feng, X., Qu, Z., Lu, X., Zhang, J., Zhu, R., Zhou, Q., He, A., Zhang, H., & Chen, S. (2025). An array sensor for monitoring the chloride concentration profile in concrete. *Construction and Build-*

ing Materials, *478*, 141419. https://doi.org/10.1016/j.conbuildmat.2025.141419

Yu, G., & Adeli, H. (1993). Object-oriented finite element analysis using EER model. *Journal of Structural Engineering*, *119*(9), 2763–2781. https://doi.org/10.1061/(ASCE)0733-9445(1993)119:9(2763)

Zhao, Y., Chen, C., Gao, X., & Jin, W. (2013). Seasonal variation of surface chloride ion content and chloride diffusion coefficient in a concrete dock. *Advances in Structural Engineering*, *16*(2), 395–403. https://doi.org/10.1260/1369-4332.16.2.395

How to cite this article: Li, Y., & Vořechovský, M. (2025). Data-driven dynamic mode decomposition framework for spatio-temporal prediction of concrete chloride ingress. *Computer-Aided Civil and Infrastructure Engineering*, *40*, 6305–6323. https://doi.org/10.1111/mice.70161